

# Hydrocyclone-enhanced Scalable Photocatalytic Hydrogen Generation: From Macroscale Turbulence to Nanoscale Reaction Dynamics

Corresponding Author: Professor Xuejing Yang

This file contains all reviewer reports in order by version, followed by all author rebuttals in order by version.

Version 0:

Reviewer comments:

Reviewer #1

(Remarks to the Author)

In this work, the authors constructed a scalable hydrocyclone-based photocatalytic reactor toward hydrogen production with a solar-to-hydrogen (STH) efficiency of 5.26%, which is 4.5 times higher than that under static conditions. Moreover, the authors developed a hierarchical multiscale framework model to bridge the macro-scale strain under hydrocyclone flow field with the atomic-level photocatalytic process. In my opinion, the use of a hydrocyclone to mitigate mass transfer limitations in conventional systems is innovative and impactful. The establishment of a force–chemical coupling mechanism through a multiscale physics framework offers an important conceptual foundation for scaling up photocatalytic processes. Therefore, I would suggest the acceptance of the manuscript in Nature Communications after the authors have addressed the following minor issues.

1. The experimental design is commendable, sustaining stable hydrogen production for 42 hours of continuous operation—a notable achievement for scaled photocatalytic systems. Further details are needed regarding the gas collection methodology and the exact procedures for determining hydrogen yield over extended operation.
2. The incorporation of a 4 °C cooling water loop demonstrates careful consideration of thermal management, a factor often overlooked in laboratory-scale studies. A temperature–time profile should be provided to confirm thermal stability and exclude local heating effects as a contributing factor to the observed performance enhancement.
3. In Figure 1f, the operational hydrocyclone-based reactor is shown in use. Dimensional annotations would help convey the actual scale of the system.
4. The multiscale modeling framework effectively integrates macroscopic fluid dynamics with nanoscale electronic processes. The discussion should address whether catalyst lattice deformation influences the d-band center position, as such shifts could be critical to understanding changes in the electronic structure.
5. The introduction presents the historical development of hydrocyclone technology. This section could be strengthened by explicitly distinguishing the present application from conventional separation processes and highlighting how the proposed force–chemical coupling strategy uniquely enables photocatalytic enhancement.

Reviewer #2

(Remarks to the Author)

This manuscript presents an innovative interdisciplinary study that combines hydrocyclone technology with photocatalytic hydrogen production through a comprehensive multiscale modeling framework. The authors demonstrate remarkable innovation by establishing a force-chemical coupling mechanism spanning from macroscale fluid dynamics to nanoscale electronic phenomena. The achievement of 5.26% solar-to-hydrogen efficiency represents a significant breakthrough that meets the threshold for industrial viability. The work exhibits outstanding scientific rigor in both experimental design and theoretical analysis, providing valuable insights for the rational design and scale-up of photocatalytic reactors. The multiscale approach from reactor-scale hydrodynamics to atomic-level strain engineering offers a new paradigm for process intensification in renewable energy applications. Thus, I recommend this manuscript for publication in Nature Communications after some minor revisions.

1. The authors have presented a very interesting multiscale force-chemical coupling modeling framework. I suggest they should provide more discussions to compare this framework with other methods. I think this would further highlight the novelty of this work.
2. Catalyst structural characterization should be more comprehensive. Solid-state nuclear magnetic resonance (NMR) and Brunauer-Emmett-Teller (BET) surface area analysis can be included to provide a more detailed understanding of the COF's porosity and structural integrity.
3. Will long-term hydrocyclone reaction conditions lead to degradation of the catalyst? Structural integrity data (XRD and XPS analyses) of the COF catalyst pre- and post- hydrocyclone reaction conditions should be supplemented.
4. The computational model employs Pt<sub>4</sub> clusters, while experimental observations show >10 nm particles with (111) facets. Could the authors provide justification for this model choice and discuss how cluster size might affect the predicted strain-induced electronic effects?
5. The manuscript mentions catalyst particle agglomeration during operation. Could the authors provide particle size distribution analysis comparing pre- and post-reaction samples to quantify agglomeration kinetics and its correlation with long-term performance stability?
6. Will the strain-induced lattice distortion also induces intramolecular charge transfer within the COF?
7. The COF structure differs from that of sodium alginate, which was used for the tracer particles in this paper. Would this hydrogel tracers exhibit equivalent hydrodynamic behavior to COF particles under the experimental flow conditions?
8. The meso-scale model in Fig. 3 contains 119 sub-particles. Will the spatial arrangement or packing structure of these sub-particles influence the computational results?
9. At the macro-scale, the forces acting on particles are random. Could the use of average force values in the calculations introduce significant errors in the multiscale modeling framework?
10. Some typos should be corrected. For example, in line 543 of the manuscript, "...together with 317 mg (1.8 mol) of ascorbic acid as a sacrificial agent..." should actually be 1.8 mmol.

#### Reviewer #3

##### (Remarks to the Author)

In this work, authors constructed a scalable 30 hydrocyclone-based photocatalytic reactor toward hydrogen production, claiming a rate of 270 mL/h 31 with a solar-to-hydrogen (STH) efficiency of 5.26%, which is 4.5 times higher than that 32 under static conditions. Author developed a hierarchical multiscale framework model which combines computational fluid dynamics, solid mechanics, and density functional theory to bridge the macro-scale strain under hydrocyclone flow field with the atomic-level photocatalytic process. From Theoretical calculations, authors predicted that stress-induced nano-scale lattice restructuring of catalyst particles modulates photoexcitation pathways, generating a threshold-activated catalytic amplification effect.

This work is having technological importance in the pursuit of renewable energy utilization. Experimental data are supported with multi-scale modelling data. Although the presentation of the data is good, simulations did not reflect rigorous professional accuracy. Also there are few issues require clear explanations. I feel, the manuscript requires a major revision on the following points:

1. The strain can introduce polarization and hence electric field in the system. It will be good to compute the induced electric field at different strain using DFT(VASP) simulations.
2. What is the Pt concentration on COF- The changes in electronic properties of COF due to Pt nano-particles need to be brought through DOS & bandstructure plots to correlate its effect on H<sub>2</sub> production.
3. Is the plane wave cut-off energy of 450 eV is sufficient? Authors should do a convergence test for the plane wave?
4. K-Point mesh of 2×2×1 k-mesh may not be sufficient-author should do a convergence test for the K-Point mesh
5. Author should mention the value of zero point energy and entropy correction in Equ\_10.
6. Surprisingly, reference for the VASP code as well as exchange correlation functionals are missing.
7. Force convergence criteria of 0.02 eV/Angs may not be very accurate-author should atleast take 0.01 eV/Angs.
8. Authors mentioned that, "each configuration running for 1,000 steps before incrementally expanding the lattice by 2% biaxially"- Is 1 ps (1000 fs) is enough to reach equilibrium before increasing the strain.
9. Is 11% strain is within the elastic limit? Is it possible to check dynamic stability at 7% strain through phonon calculations.
10. For the AIMD structures, author need to show energy fluctuation and bond length fluctuations with different strain

Version 1:

Reviewer comments:

Reviewer #1

(Remarks to the Author)

The authors have addressed my concerns and I would suggest the acceptance of the work.

Reviewer #2

(Remarks to the Author)

I think that the authors of this manuscript have carefully addressed all my concerns and it can be accepted for publication in my view.

Reviewer #3

(Remarks to the Author)

Authors have revised the manuscript reasonably well. It may be accepted now.

**Open Access** This Peer Review File is licensed under a Creative Commons Attribution 4.0 International License, which permits use, sharing, adaptation, distribution and reproduction in any medium or format, as long as you give appropriate credit to the original author(s) and the source, provide a link to the Creative Commons license, and indicate if changes were made.

In cases where reviewers are anonymous, credit should be given to 'Anonymous Referee' and the source.

The images or other third party material in this Peer Review File are included in the article's Creative Commons license, unless indicated otherwise in a credit line to the material. If material is not included in the article's Creative Commons license and your intended use is not permitted by statutory regulation or exceeds the permitted use, you will need to obtain permission directly from the copyright holder.

To view a copy of this license, visit <https://creativecommons.org/licenses/by/4.0/>

# **Hydrocyclone-enhanced Scalable Photocatalytic Hydrogen Generation: From Macroscale Turbulence to Nanoscale Reaction Dynamics**

Corresponding author: Jianping Li, Xuejing Yang, Hualin Wang.

E-mail address:

[lijianping1016@scu.edu.cn](mailto:lijianping1016@scu.edu.cn) (J.L.)

[xj.yang@ecust.edu.cn](mailto:xj.yang@ecust.edu.cn) (X.Y.).

[wanghl@ecust.edu.cn](mailto:wanghl@ecust.edu.cn) (H.W.).

**Reviewer #1 (Remarks to the Author):**

In this work, the authors constructed a scalable hydrocyclone-based photocatalytic reactor toward hydrogen production with a solar-to-hydrogen (STH) efficiency of 5.26%, which is 4.5 times higher than that under static conditions. Moreover, the authors developed a hierarchical multiscale framework model to bridge the macro-scale strain under hydrocyclone flow field with the atomic-level photocatalytic process. In my opinion, the use of a hydrocyclone to mitigate mass transfer limitations in conventional systems is innovative and impactful. The establishment of a force–chemical coupling mechanism through a multiscale physics framework offers an important conceptual foundation for scaling up photocatalytic processes. Therefore, I would suggest the acceptance of the manuscript in Nature Communications after the authors have addressed the following minor issues.

**Response:**

Thank you very much for your positive and encouraging feedback on our manuscript. We are delighted that you recognize our work on multiscale hydrogen-production engineering. Your comments are invaluable and have helped us strengthen the scientific rigor and completeness of the study.

1. The experimental design is commendable, sustaining stable hydrogen production for 42 hours of continuous operation—a notable achievement for scaled photocatalytic systems. Further details are needed regarding the gas collection methodology and the exact procedures for determining hydrogen yield over extended operation.

**Response:**

Thank you for this helpful suggestion. We have added a detailed description of our gas-collection and yield-quantification protocol, summarized below and incorporated into the **Experimental methods in Supporting Information (page 7)**.

**Headspace definition and calibration.**

Prior to each run, the reactor is completely filled with the preset feed solution (~20 L prepared in advance) while the circulation pump is operated at a low flow rate to remove residual bubbles, until overflow occurs and the internals are fully liquid-filled.

We then open the bottom drain valve and withdraw 500 mL of liquid using a calibrated volumetric cylinder, which defines a fixed gas headspace of  $V_{\text{HS}} = 500 \text{ mL} \pm 5 \text{ mL}$ . This “calibrated volumetric displacement” avoids ambiguity associated with informal “water-displacement” wording.

### **Sampling and analysis.**

At a given time  $t_k$ , we sample 1 mL of the headspace using a gas-tight microsyringe and record the headspace absolute pressure  $P_k$  from the in-line gauge and the temperature  $T_k$ . The sample is injected into the gas chromatograph, and the  $\text{H}_2$  mole fraction  $y_k$  is obtained from a calibration curve. The instantaneous moles of hydrogen

in the headspace are computed with the ideal-gas relation:

$$n_k(\text{H}_2) = \frac{(P_k - P_{\text{H}_2\text{O}}(T_k)) V_{\text{HS}}}{RT_k} \times y_k \quad (\text{R1})$$

where  $P_{\text{H}_2\text{O}}(T_k)$  is the saturated water-vapor pressure at  $T_k$  and  $R$  is the gas constant. The 1 mL sampling volume is  $<0.2\%$  of  $V_{\text{HS}}$ ; we correct  $P_k$  and  $y_k$  for this removal in the data reduction.

These methodological details have been incorporated into the Supporting Information (Experimental Procedures) to provide the key information necessary for independent replication and reproducibility of our results.

### **Yield and rate over extended operation.**

Measurements are taken every 30 min. The cumulative hydrogen yield over any interval is evaluated as the telescoping sum of headspace increases:

$$N_{\text{H}_2}(t_j) = \sum_{k=1}^j [n_k(\text{H}_2) - n_{k-1}(\text{H}_2)] \quad (\text{R2})$$

and the average production rate over  $[t_{k-1}, t_k]$  is  $r_k = (n_k - n_{k-1})/\Delta t$ . To prevent saturation and to maintain consistent sensitivity, operation is organized into 3.5 h cycles (8 analyses per cycle). At the end of each cycle, the headspace is purged with

Ar for 10 min to reduce residual H<sub>2</sub>; the first analysis of the next cycle defines the new baseline ( $n_0 \approx 0$ ). The hydrogen removed during purge is accounted for by closing the material balance on each cycle.

2. The incorporation of a 4 °C cooling water loop demonstrates careful consideration of thermal management, a factor often overlooked in laboratory-scale studies. A temperature–time profile should be provided to confirm thermal stability and exclude local heating effects as a contributing factor to the observed performance enhancement.

**Response:**

Thank you for emphasizing the importance of thermal management. A temperature-time profile has been incorporated, and the experimental methodology has been expanded upon in the Supporting Information.

Because the reactor operates under high-turbulence recirculation, we reasonably assume that the solid–liquid phases are well mixed and that the recirculation loop remains effectively isothermal during operation. The following methods are supplemented in **Experimental methods of Supporting Information (page 8)**: A temperature probe mounted on the reservoir recorded the bulk liquid temperature every 30 min. With the chiller supplying cooling water at 4 °C, the illuminated reactor maintained a stable bulk temperature of  $30 \pm 1$  °C. Representative temperature–time traces from three independent runs (September 18, 22, and 25, 2025) show that thermal steady state is reached within ~2 h after start-up and exhibits no drift during extended operation. This stable, near-ambient bulk temperature under strong convective mixing supports that the observed performance enhancement does not originate from local photothermal heating. The relevant discussion has been added in the **revised manuscript (line 135-136)**: “...control for the reactor. The reaction solution was able to maintain a stable temperature of  $30 \pm 1$  °C with the help of a cooling system to exclude local thermal effects (Fig. S3, shown as Fig. R1). The photocatalytic fluid loop includes...”

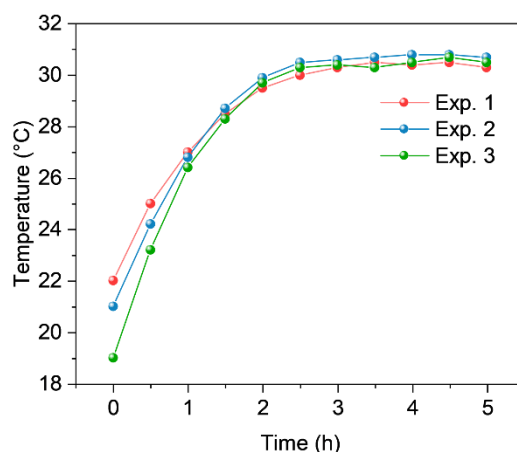


**Fig. R1** Temperature evolution of the reaction liquid.

3. In Figure 1f, the operational hydrocyclone-based reactor is shown in use. Dimensional annotations would help convey the actual scale of the system.

**Response:**

Thank you for the helpful suggestion. We have added a dimensioned schematic of the hydrocyclone-based reactor as Fig. S2 (shown as Fig. R2) in the **Supporting Information (page 10)**, including the overall footprint and height as well as key component dimensions to convey the system's true scale. Reference added in **revised manuscript (line 132)**: “more details about the reactor can be found in Fig. S1 and S2”

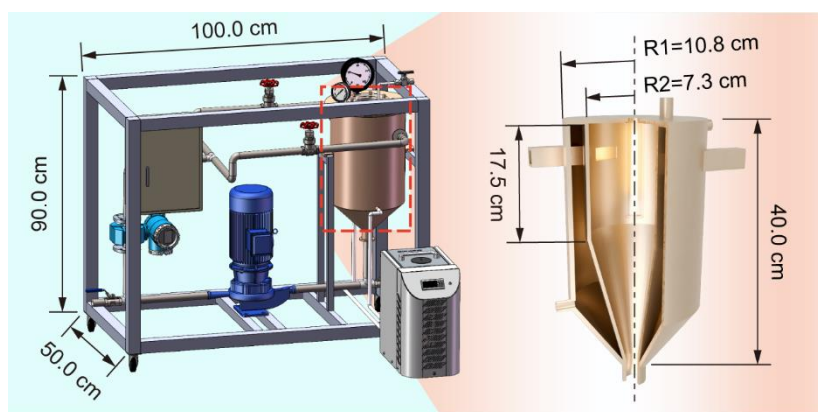


**Fig. R2** Dimensioned schematic of the hydrocyclone-based photocatalytic reactor.

4. The multiscale modeling framework effectively integrates macroscopic fluid dynamics with nanoscale electronic processes. The discussion should address whether catalyst lattice deformation influences the d-band center position, as such shifts could be critical to understanding changes in the electronic structure.

**Response:**



Thank you for this insightful comment, we evaluated the d-band center across five in-plane strain levels (0–9%; Fig. S22, shown as Fig. R3). We quantified how lattice deformation affects the electronic structure by computing the Pt-site d-band center across five in-plane tensile strains (0–9%). As shown in Fig. S23(a) (shown as Fig. R4(a)),  $\varepsilon_d$  increases approximately linearly with strain up to ~7%, but turns over at 9%. In the same strain range,  $\Delta G_{H^*}$  co-varies with  $\varepsilon_d$  broadly consistent with the classic d-band picture. Notably, the ~7% case deviates from the linear trend: although  $\varepsilon_d$  is upshifted,  $\Delta G_{H^*}$  becomes larger Fig. S23(b) (shown as Fig. R4 (b)). PDOS overlays indicate progressive band narrowing and peak isolation at 7–9%, evidencing state localization/symmetry breaking near the Pt–COF junction; under these conditions the single-parameter  $\varepsilon_d$  alone is insufficient to predict adsorption energetics.

We therefore conclude that when  $\varepsilon_d$  remains below 0 eV (modest strain), the strain–activity trend is broadly consistent with the classic d-band picture; however, at larger strain—where  $\varepsilon_d$  upshifts and the spectrum becomes more localized—the observed HER enhancement is explained in the main text by changes in excited-state character rather than by the d-band center alone. We have therefore included the above description in the **revised manuscript (line 459-467)**: “To connect the excited-state picture with steady-state reactivity, we first examined the  $\varepsilon_d$  descriptors under strain (Fig. S22). As shown in Fig. S23(a),  $\varepsilon_d$  increases approximately linearly with strain up to ~7%, but turns over at 9%. In the same strain range,  $\Delta G_H$  co-varies with  $\varepsilon_d$  broadly consistent with the classic d-band picture. Notably, the ~7% case deviates from the linear trend: although  $\varepsilon_d$  is upshifted,  $\Delta G_H$  becomes larger (Fig. S24(b)). These results indicate that, while the d-band descriptor tracks the activity trend at modest strain, it becomes insufficient at larger strain. Therefore, it is necessary to provide more direct evidence via thermodynamic H-adsorption calculations on Pt sites.”

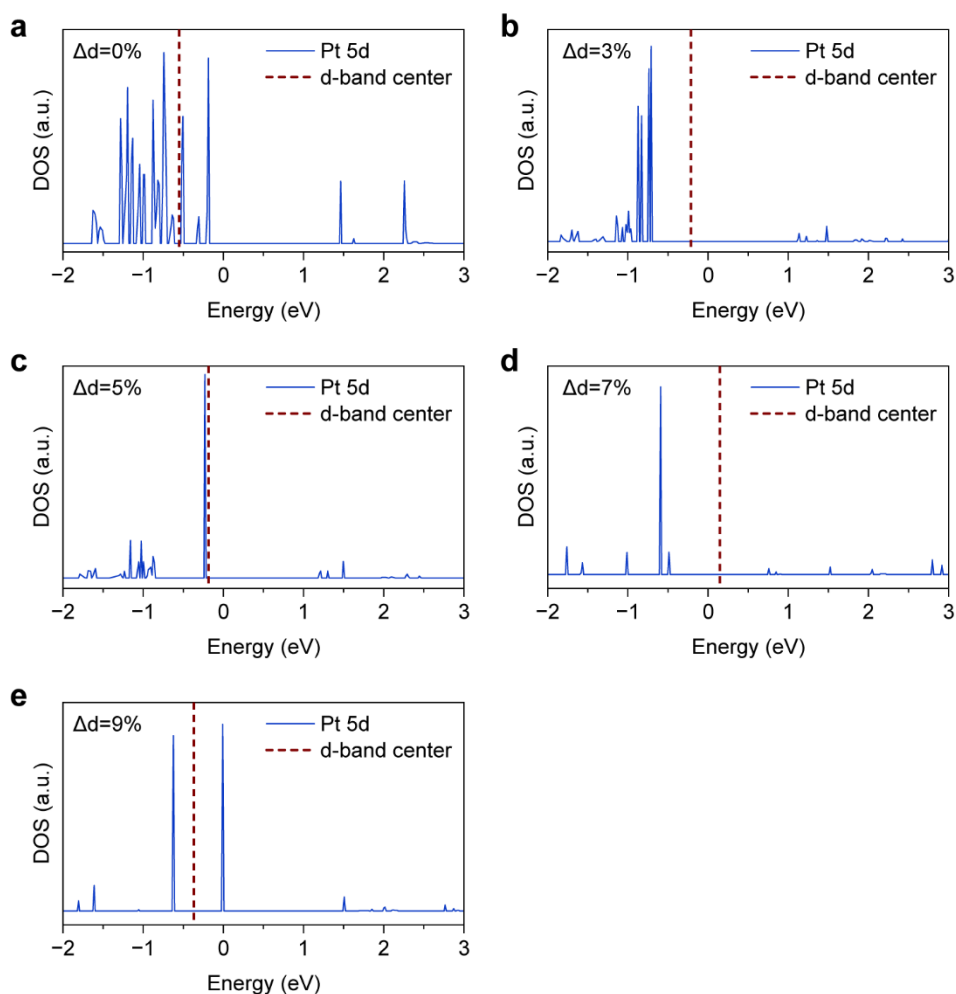


**Fig. R3** DOS of Pt-COF under different lattice strains.

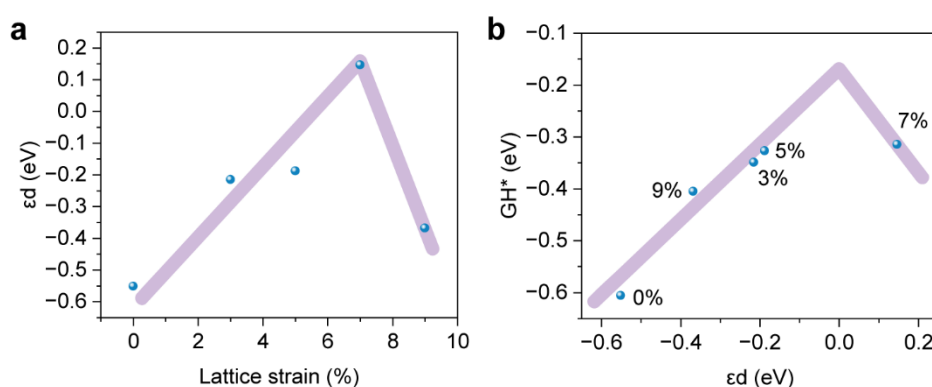


**Fig. R4** (a) d-band center versus lattice strain; (b) Relationship between d-band center and  $GH^*$ .

Qiao Z, Jiang R, Yun J, et al. Why the abnormal phenomena of D-band center theory exist? A new BASED theory for surface catalysis and chemistry. Chinese Journal of Catalysis, 2024, 64: 44-53.

5. The introduction presents the historical development of hydrocyclone technology.

This section could be strengthened by explicitly distinguishing the present application from conventional separation processes and highlighting how the proposed force–chemical coupling strategy uniquely enables photocatalytic enhancement.

**Response:**

Thank you for this constructive suggestion. The Introduction has been revised to explicitly distinguish the present application from conventional separation-focused uses of hydrocyclones and to highlight the force–chemical coupling route that uniquely enables photocatalytic enhancement.

Specifically, we made a change **in line 81-90 of the revised manuscript:** “However, despite broad adoption as separation units, hydrocyclones are seldom treated as active reactors: systematic exploitation of their high-shear and negative-pressure core to drive hydrodynamic–chemical (force-chemical) coupling for catalytic enhancement remains scarcely addressed. Against this backdrop, the intense swirling flow and high shear forces within hydrocyclones provide an ideal platform for implementing strain engineering strategies at the catalyst level[30]. These mechanical forces cause lattice distortions, which alter the electronic structure[31], enhance surface active site reactivity, and modify charge-transfer properties in catalytic material[32], thereby improving overall catalytic performance.”

[30] Mao X, Qin Z, Ge S, et al. Strain engineering of electrocatalysts for hydrogen evolution reaction. *Materials Horizons*, 2023, 10(2): 340-360.

[31] Chen K, Li G, Gong X, et al. Atomic-scale strain engineering of atomically resolved Pt clusters transcending natural enzymes. *Nature Communications*, 2024, 15(1): 8346.

[32] Lin J, Zhang N. Constructing strain in electrocatalytic materials for CO<sub>2</sub> reduction reactions. *Green Chemistry*, 2024.

## Reviewer #2 (Remarks to the Author):

This manuscript presents an innovative interdisciplinary study that combines hydrocyclone technology with photocatalytic hydrogen production through a comprehensive multiscale modeling framework. The authors demonstrate remarkable innovation by establishing a force chemical coupling mechanism spanning from macroscale fluid dynamics to nanoscale electronic phenomena. The achievement of 5.26% solar-to-hydrogen efficiency represents a significant breakthrough that meets the threshold for industrial viability. The work exhibits outstanding scientific rigor in both experimental design and theoretical analysis, providing valuable insights for the rational design and scale-up of photocatalytic reactors. The multiscale approach from reactor-scale hydrodynamics to atomic-level strain engineering offers a new paradigm for process intensification in renewable energy applications. Thus, I recommend this manuscript for publication in Nature Communications after some minor revisions.

## Response:

Thank you very much for the positive evaluation, especially your recognition of our work on the design of a scalable photocatalytic reactor. Your suggestions were essential to our revisions.

1. The authors have presented a very interesting multiscale force-chemical coupling modeling framework. I suggest they should provide more discussions to compare this framework with other methods. I think this would further highlight the novelty of this work.

## Response:

Thank you for your suggestion, and we have added a summary and discussion of multiscale modelling based on your suggestion, specifically **in line 373-376 of the revised manuscript**: "...nano-scales through displacement. Crucially, the formulation establishes an explicit load-transfer pathway from reactor-scale hydrodynamics (CFD-DEM) to nanoscale lattice states (DFT): hydrodynamic velocity/pressure fields define mesoscopic stress boundary conditions (FEM), which are propagated as resolved strain/displacement fields to the atomistic model. As a result, the..."

2. Catalyst structural characterization should be more comprehensive. Solid-state

nuclear magnetic resonance (NMR) and Brunauer-Emmett-Teller (BET) surface area analysis can be included to provide a more detailed understanding of the COF's porosity and structural integrity.

**Response:**

Thank you for the suggestion. We have added solid-state  $^{13}\text{C}$  NMR to confirm the successful synthesis of the COFs and the presence of the characteristic  $\beta$ -ketoenamine linkages (Fig. S7, shown as Fig. R5). Additionally, add the following description to **line 235-238 in the revised manuscript**: “...and in parallel solid-state  $^{13}\text{C}$  NMR verifies successful COF formation with characteristic  $\beta$ -ketoenamine linkages (Fig. S7, shown as Fig. R5).”

We have also included  $\text{N}_2$  adsorption–desorption analysis at 77 K with BET surface area determination (Fig. S8, shown as Fig. R6), together with the corresponding numerical data. Additionally, add the following description to **line 238-240 in the revised manuscript**: “...Finally,  $\text{N}_2$  sorption/BET analysis (Fig. S8, shown as Fig. R6) reveals a surface-area decrease upon Pt loading (from 964.0 to 475.9  $\text{m}^2/\text{g}$ ), consistent with partial micropore blocking by deposited Pt NPs.”

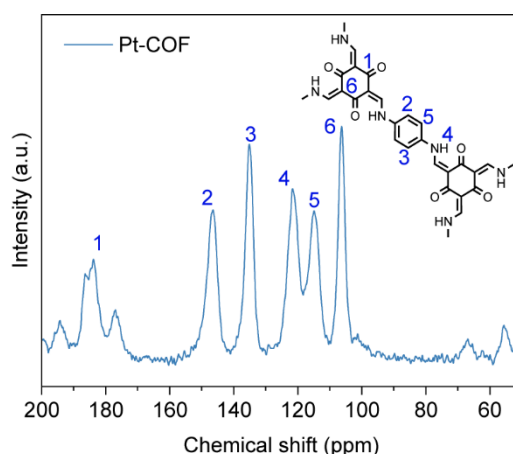


**Fig. R5** Solid-state CP-MAS  $^{13}\text{C}$  NMR spectra of Pt-COF.

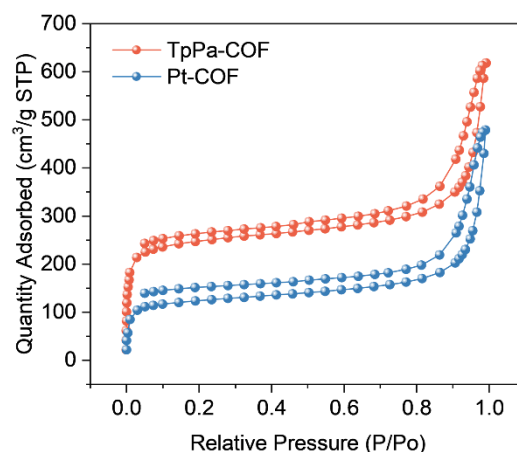


**Fig. R6** N<sub>2</sub> adsorption and desorption isotherms (77 K) of TpPa-COF and Pt-COF.

3. Will long-term hydrocyclone reaction conditions lead to degradation of the catalyst? Structural integrity data (XRD and XPS analyses) of the COF catalyst pre- and post hydrocyclone reaction conditions should be supplemented.

**Response:**

Thank you for your advice. We have supplemented pre- and post-hydrocyclone structural characterizations of the catalyst, including powder XRD (Fig. S10, shown as Fig. R7) and high-resolution XPS (Fig. S6, shown as Fig. R8). The XRD patterns show no emergence of new reflections and no measurable shifts in the principal COF peaks, indicating preservation of the primary crystalline framework. Consistently, XPS reveals no binding-energy shifts in Pt 4f and N 1s before vs. after operation, supporting chemical-state stability of both the Pt species and the COF linkages. These results together confirm good structural integrity of the catalyst under long-term hydrocyclone conditions.

We added the thesis in **line 254-257 of the revised manuscript**: “Concurrently, XRD (Fig. S10) and XPS analyses (Fig. S6) conducted prior to and following extended hydrocyclone operation revealed no occurrence of new phases or discernible binding energy shifts, thereby substantiating the structural and chemical stability of the Pt-COF.”

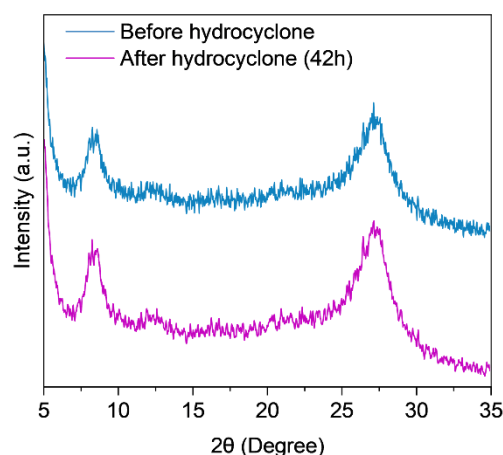


**Fig. R7** XRD of Pt-COF before and after hydrocyclone operation.

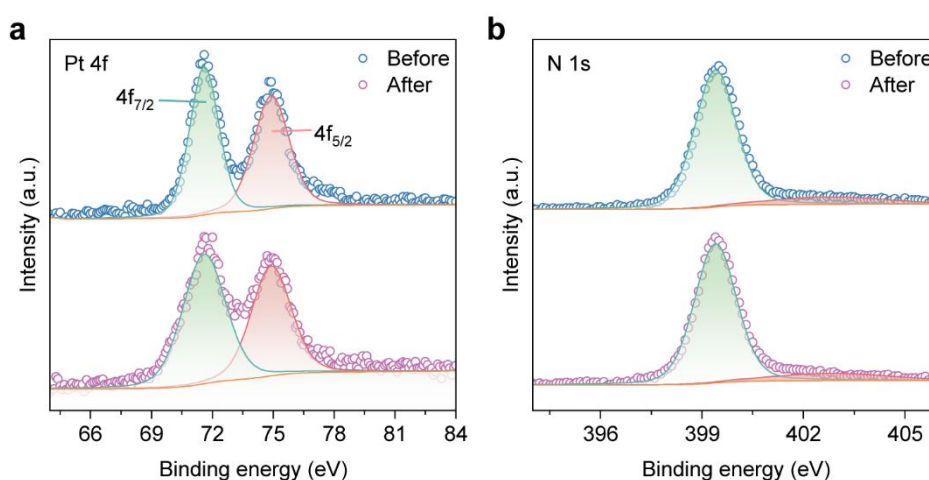


**Fig. R8** XPS spectra of Pt-COF before and after hydrocyclone operation: (a) Pt 4f and (b) N 1s.

4. The computational model employs Pt<sub>4</sub> clusters, while experimental observations show >10 nm particles with (111) facets. Could the authors provide justification for this model choice and discuss how cluster size might affect the predicted strain-induced electronic effects?

**Response:**

Thank you for raising this important point. Our DFT model employs a Pt<sub>4</sub> cluster as a site-specific interfacial surrogate rather than a morphological replica of the >10 nm Pt (1 1 1) particles. This is a standard choice when the objective is to capture local electronic polarization, ligand–metal charge redistribution (LMCT), and strain sensitivity at the photocatalytically active COF–Pt junction with tractable computational cost. The chemical relevance and stability of few-atom Pt motifs (single

atoms, dimers, and small clusters) on carbonaceous or N-rich supports are well documented in hydrogen photocatalysis, providing an experimentally grounded basis for such surrogates.

Regarding stability and modeling rationale, prior first-principles studies report that Pt<sub>4</sub> adopts compact (tetrahedral-like) minima on supports and remains structurally robust under reactive conditions, while serving as a tractable proxy for probing elementary steps and electronic descriptors. Consistent with this, our AIMD simulations under in-plane strain show that the Pt<sub>4</sub> motif retains its tetrahedral character throughout the deformation window considered. Taken together, these considerations motivate our use of Pt<sub>4</sub> in lieu of an extended nanoparticle model. We emphasize that our conclusions concern local strain–polarization couplings and descriptor trends pertinent to photocatalytic charge separation and HER, rather than absolute particle morphology.

Based on the above arguments, we have supplemented our modeling explanation **in line 409-414 of the revised manuscript**: “Informed by prior work on few-atom Pt ensembles in photocatalysis, we model the COF–Pt junction using a Pt<sub>4</sub> interfacial surrogate to resolve site-specific, strain-sensitive electronic responses at under-coordinated motifs, rather than reproducing the global morphology of >10 nm Pt (1 1 1) particles. This surrogate is chemically relevant and computationally tractable, and it preserves the polarization physics central to our photoinduced mechanism[53].”

[53] Li Y, Yang L, He H, et al. In situ photodeposition of platinum clusters on a covalent organic framework for photocatalytic hydrogen production. *Nature Communications*, 2022, 13(1): 1355.

5. The manuscript mentions catalyst particle agglomeration during operation. Could the authors provide particle size distribution analysis comparing pre- and post-reaction samples to quantify agglomeration kinetics and its correlation with long-term performance stability?

**Response:**

Thank you for this valuable suggestion. We have added particle size distribution (PSD) measurements of the actual reaction slurry taken during long-cycle operation at 8 h, 16 h, and 24 h using a Malvern laser diffraction analyzer (Fig. S9 shown as Fig.



R9). The results show that, as operation proceeds, the fraction of single particles and small agglomerates increases, while the fraction of large agglomerates decreases—consistent with shear in the hydrocyclone flow suppressing particle agglomeration. This mechanistic picture explains why our hydrocyclone reactor sustains stable operation longer than conventional static photoreactors. Based on the above discussion, we add in **line 247-251 of the revised manuscript**: “Volume-weighted PSDs of the reaction slurry at 8, 16, and 24 h (Fig. S9 shown as Fig. R9) show a time-dependent increase in single/small-agglomerate fractions and a decrease in large agglomerates, indicating that the hydrocyclone’s high-shear, rapid recirculation suppresses agglomeration. This suppression is consistent with the sustained performance observed over extended operation.”

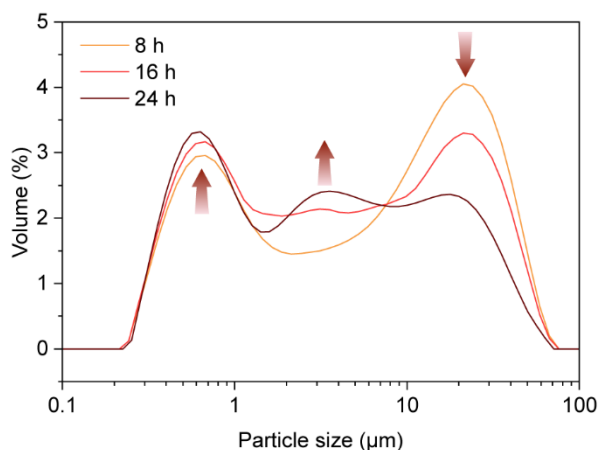


**Fig. R9** PSD of the reaction slurry at 6 h, 12 h, and 18 h measured by Malvern laser diffraction.

6. Will the strain-induced lattice distortion also induce intramolecular charge transfer within the COF?

**Response:**

Thank you for the comment. Our excited-state analysis focuses on the COF/Pt interface. In the original manuscript we compared Pt-loaded structures at 5% and 7% strain and found a strain-induced shift from local excitation (LE) to ligand-to-metal charge transfer (LMCT). The additional calculations clarify the limitation of the pristine COF and the decisive role of strain: at low strain, TpPa-COF and Pt-COF exhibit mixed LE/LMCT in which Pt NPs do not fully separate the intramolecularly generated charges;

with increased strain, LMCT at the COF/Pt interface becomes the dominant separation pathway, while COF-only intramolecular charge transfer is reduced to a secondary component rather than an independent channel (Fig. S21 shown as Fig. R10).

We have therefore added the following description to the **revised manuscript (line 451-454)**: “Additionally, we analyzed pristine TpPa-COF and a low-strain Pt-COF (3%) reference and found predominantly local excitations in both cases (Fig. S21). Thus, Pt loading is necessary to provide electron-acceptor states, whereas tensile strain amplifies the separation; together they couple to enable efficient electron-hole splitting.”

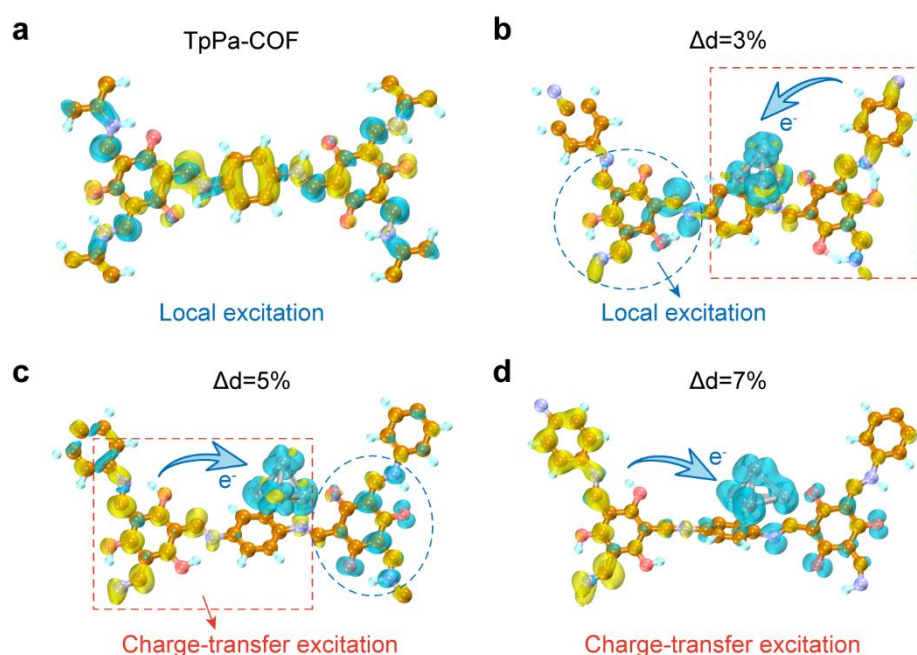


**Fig. R10** TDDFT electron-hole distributions at different lattice strains: (a) TpPa-COF, (b) 3%, (c) 5%, (d) 7%.

7. The COF structure differs from that of sodium alginate, which was used for the tracer particles in this paper. Would this hydrogel tracers exhibit equivalent hydrodynamic behavior to COF particles under the experimental flow conditions?

**Response:**

Thank you for the comments. We employed sodium-alginate hydrogel spheres solely as flow-field tracers to visualize particle kinematics and qualitatively assess shear-induced deformation in the hydrocyclone; they were not used as substitutes for the catalyst in performance tests. Importantly, compared with real COF particles, the hydrogel tracers are softer and therefore deform more readily—a property that aids

visualization but precludes any one-to-one quantification of COF deformation. Our objectives were to track particle translational–rotational kinematics (flow following, entry into and residence within the low-pressure core, helical trajectories) and use the deformable tracer to indicate the direction and onset of deformation in high-shear zones, rather than to measure the absolute deformation of COF particles.

We have therefore amended our description in the **revised manuscript (line 278-281)**: “...under hydrocyclonic conditions. The sodium-alginate polymer tracers were density-matched to the catalyst particles. Because their elastic modulus is lower than that of the COF particles, they permit qualitative evaluation of shear-induced deformation in the hydrocyclone while maintaining catalyst-like flow behavior[49]. These tracer particles...”

[49]Yuan X, Li B, Huang Y, et al. Progress in preparation and application of sodium alginate microcapsules. Chemical Industry and Engineering Progress, 2021, 41(6): 3103.

8. The meso-scale model in Fig. 3 contains 119 sub-particles. Will the spatial arrangement or packing structure of these sub-particles influence the computational results?

**Response:**

We are grateful for the insightful inquiry. We have contemplated the potential impact of sub-particle spatial configuration on the computational outcomes. To this end, we have devised and computed six distinct models, wherein the particle positions are randomly dispersed (Fig. S11 shown as Fig. R11). The comparison reveals that when the number of sub-particles is approximately 120, the computational results manifest commendable stability and consistency. Consequently, we contend that the meso-scale model employed in this study is both reliable and representative.

We have supplemented the particle modelling algorithm in **Theory and Formula of Supporting Information (page 3)**:

**Particle-packing model (Dense Sphere Packing, DSP)**

We generated random, non-overlapping sphere packings in a cubic RVE ( $V_{\text{RVE}} = L^3$ ) using Digimat’s DSP algorithm. For a prescribed radius set  $\{r_i\}_{i=1}^N$  and target

packing fraction  $\phi_{\text{target}}$ , the configuration satisfies:

### Packing fraction

$$\phi = \frac{1}{V_{\text{RVE}}} \sum_{i=1}^N \frac{4}{3} \pi r_i^3 \approx \phi_{\text{target}} \quad (\text{R3})$$

### Non-overlap

$$\| \mathbf{x}_i - \mathbf{x}_j \|_{\min} \geq r_i + r_j \quad (\forall i \neq j) \quad (\text{R4})$$

The algorithm iteratively relaxes sphere positions until the non-overlap constraint is met and  $|\phi - \phi_{\text{target}}| \leq \varepsilon_\phi$ . Compared with Random Sequential Addition (RSA), DSP more reliably reaches higher  $\phi$  while maintaining randomness, making it suitable for representative RVEs.

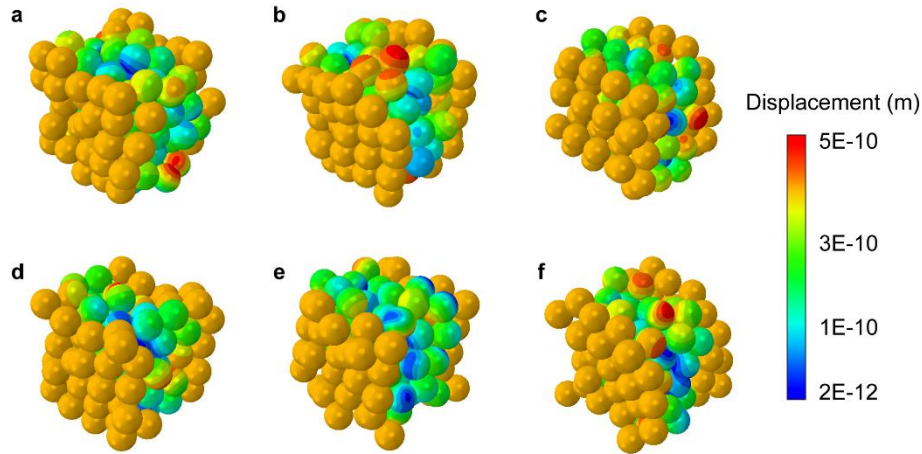


**Fig. R11** Agglomerate displacement across six independent realizations.

9. At the macro-scale, the forces acting on particles are random. Could the use of average force values in the calculations introduce significant errors in the multiscale modeling framework?

### Response:

We are grateful for your perspicacious commentary. In the present study, our main objective is to investigate the overall influence of flow velocity on particle behavior at the macro-scale, rather than capturing the instantaneous fluctuations of individual particle-fluid interactions. For this purpose, the use of the average force values (Equation R5) is considered more representative, since it reflects the effective loading

state imposed by a given flow velocity.

$$\bar{F}_i = \frac{1}{N_t} \sum_{k=1}^{N_t} F_i(t_k) \quad (\text{R5})$$

It should also be noted that the maximum forces exhibit strong randomness, which may not faithfully characterize the actual load level corresponding to a specific flow velocity. In contrast, averaging the forces over multiple particles and time steps provides a statistically meaningful measure of the effective driving force, thereby avoiding biased interpretations due to extreme values. Moreover, several related studies have also employed averaged physical quantities (such as mean velocity and mean drag force) to characterize the flow field and particle behavior, rather than relying on instantaneous values. This approach effectively captures the statistical equilibrium of the system and provides a robust representation of the flow-particle interactions at the macro scale. Therefore, we believe that adopting average force values does not introduce significant errors in the multiscale framework, but instead enhances the robustness of the model in representing the flow-induced loading conditions.

We provide additional explanation in **Theory and Formula of Supporting Information (page 3):**

#### **Note on averaged force**

To represent the macro-scale loading imposed by a given flow velocity, we use the time-averaged force for component  $i$ :

$$\bar{F}_i = \frac{1}{N_t} \sum_{k=1}^{N_t} F_i(t_k) \quad (\text{R5})(5)$$

where  $F_i(t_k)$  is the instantaneous force sampled at times  $t_k$  over a statistically steady window of length  $N_t$ . This time average filters out high-frequency fluctuations that are not resolved at the macro scale and yields an effective driving load associated with the operating condition. In contrast, instantaneous or maximum forces can be strongly intermittent and may overstate the typical load for a fixed velocity. We therefore report  $\bar{F}_i$  as the primary descriptor, together with its sampling uncertainty.

10. Some typos should be corrected. For example, in line 543 of the manuscript, "...together with 317 mg (1.8 mol) of ascorbic acid as a sacrificial agent..." should

actually be 1.8 mmol.

**Response:**

Thank you for pointing out the error for us; the relevant discussion has been corrected in **line 588-589 of the revised manuscript**: "...in this work. First, a precursor solution was prepared by dispersing 540 mg of catalyst in 500 mL of ultrapure water, together with 317 mg (1.8 mmol) of ascorbic acid as a sacrificial agent; the mixture was..."

**Reviewer #3 (Remarks to the Author):**

In this work, authors constructed a scalable hydrocyclone-based photocatalytic reactor toward hydrogen production, claiming a rate of 270 mL/h with a solar-to-hydrogen (STH) efficiency of 5.26%, which is 4.5 times higher than that under static conditions. Author developed a hierarchical multiscale framework model which combines computational fluid dynamics, solid mechanics, and density functional theory to bridge the macro-scale strain under hydrocyclone flow field with the atomic-level photocatalytic process. From Theoretical calculations, authors predicted that stress-induced nano-scale lattice restructuring of catalyst particles modulates photoexcitation pathways, generating a threshold-activated catalytic amplification effect.

This work is having technological importance in the pursuit of renewable energy utilization. Experimental data are supported with multi-scale modelling data. Although the presentation of the data is good, simulations did not reflect rigorous professional accuracy. Also there are few issues require clear explanations. I feel, the manuscript requires a major revision on the following points:

**Response:**

Thank you for your expert comments on the theoretical modeling. Your suggestions will undoubtedly help us build a more rigorous and scientifically sound framework. Below we provide our point-by-point responses and corresponding revisions.

1. The strain can introduce polarization and hence electric field in the system. It will be good to compute the induced electric field at different strain using DFT(VASP) simulations.

**Response:**

Thank you for this constructive suggestion. We have added electrostatic potential (ESP) maps under in-plane tensile strains from 0% to 7% (Fig. R12; color scale: blue = higher ESP, red = lower ESP). Across all strains, regions of higher ESP remain localized around the Pt nanoparticles, revealing a persistent interfacial dipole at the COF–Pt junction and indicating that moderate lattice strain induces only minor changes in the overall ESP landscape. Nevertheless, we believe that the calculation of the electrostatic

potential is essential for the identification of the HER active site, and we therefore add in **line 469-471 of the revised manuscript**: “...by the strains. First, ESP calculations (Fig. S24 shown as Fig. R12) demonstrate that the potential HER-active sites are located on the surfaces of the Pt NPs. Crystal Orbital Hamilton...” All calculations were independently performed on the same structures using CP2K 9.1 and VASP 6.4, and the results showed no significant differences.

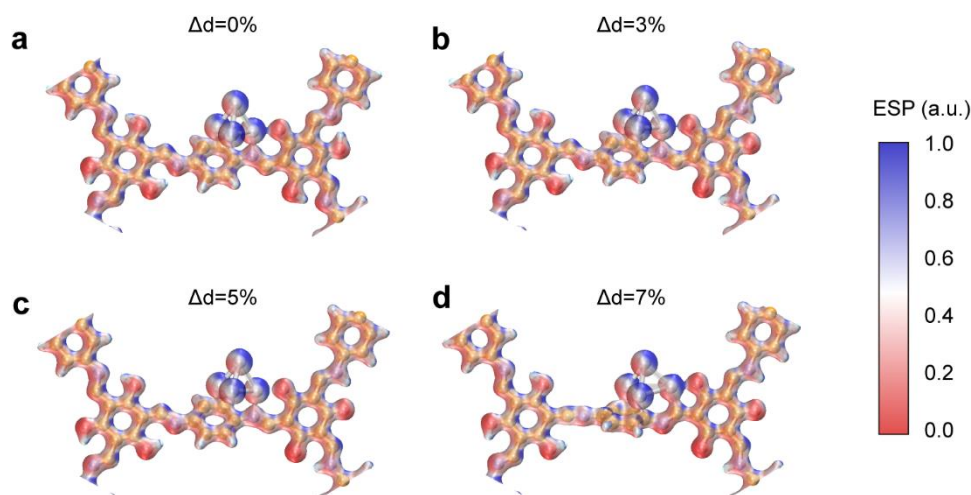


**Fig. R12** ESP calculations of different lattice strains: (a) TpPa-COF, (b) 3%, (c) 5%, (d) 7%.

2. What is the Pt concentration on COF- The changes in electronic properties of COF due to Pt nano-particles need to be brought through DOS & bandstructure plots to correlate its effect on H<sub>2</sub> production.

**Response:**

Thank you for your comments, both our EDS characterisation and the manuscript state that the Pt content is 1 wt%. The exact description is **in line 223-226 of the revised manuscript**: “...be effectively tuned. EDS mapping (Fig. S5) shows a uniform distribution of Pt, and the representative catalyst contains ~1 wt% Pt. This loading is consistent with AC HAADF-STEM images (Fig. 2d), which reveal 10-20 nm Pt domains dispersed on the COF surface. High-resolution TEM...”

To elucidate the electronic consequences of Pt loading in relation to H<sub>2</sub> production, we added DOS (Fig. S13 shown as Fig. R13) and band-structure comparisons (Fig. S12



shown as Fig. R14). Pt incorporation enriches the near-gap density of states and introduces isolated, Pt-derived dopant levels within the gap, in addition to contributing states near the Fermi level. These hybrid Pt–COF states act as electron-accepting sinks at the junction under illumination, thereby initiating and enabling HER. At the same time, the strain-dependent performance enhancement primarily arises from changes in excitation pathways and interfacial polarization (rather than gap narrowing alone), so our mechanistic explanation is complementary to, and not in conflict with, the essential kick-off role of Pt in establishing HER-active interfacial sites.

Amendments have been made to **line 391-395 of the revised manuscript**: “Conventional ground-state DFT band structures (Fig. S12) and densities of states (Fig. S13) show that Pt NPs loading introduces abundant hybrid states near the Fermi level (close to the valence-band maximum) as well as isolated in-gap levels, these states initiate HER by providing electron-accepting sinks at the COF-Pt junction. To further rationalize the experimentally observed strain-enhanced activity, we performed hierarchical multiscale modeling to quantify the strain-transmission pathway from the macroscale to the nanoscale. Fig. 4a quantifies...”

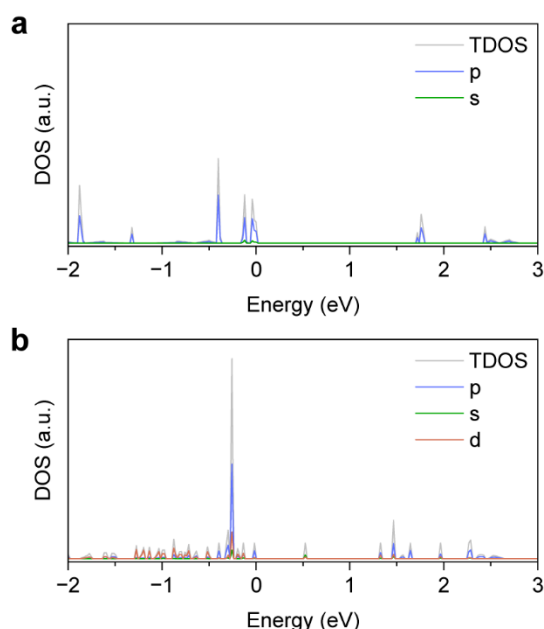


**Fig. R13** Total and projected DOS of (a) TpPa-COF and (b) Pt-COF.

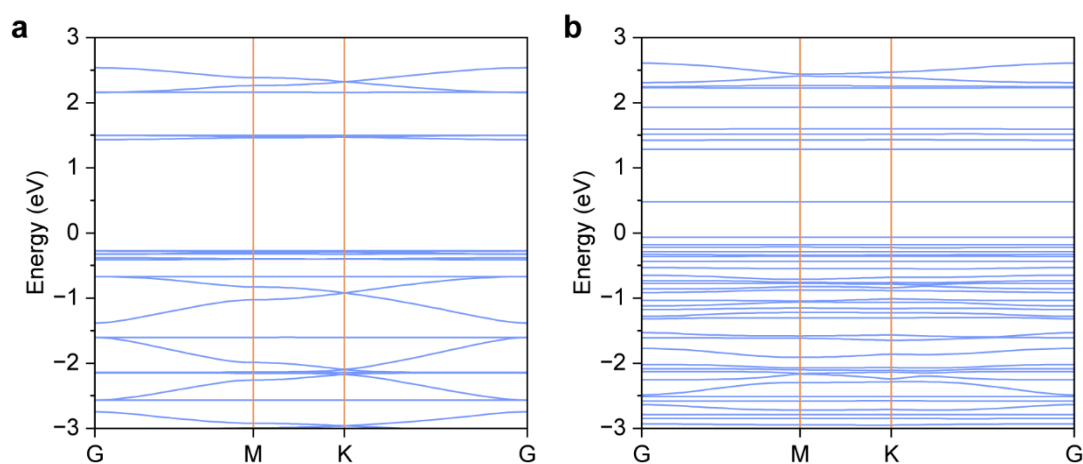


**Fig. R14** Band structures of (a) TpPa-COF and (b) Pt-COF.

3. Is the plane wave cut-off energy of 450 eV is sufficient? Authors should do a convergence test for the plane wave?

**Response:**

Thank you for your comments, your concern is reasonable, we have done the convergence test before the large-scale calculation, and we will provide the convergence data first: we can see that the cut-off energy has converged above 450 eV, and the energy fluctuation is less than 0.01 eV, so it is reasonable to take 450 eV for the calculation. The relevant data have been added to **Supporting Information** (Fig. S26 shown as Fig. R15), and an additional citation is given in **line 637-638 of the revised manuscript**: "...Convergence test data are shown in Fig. S26."

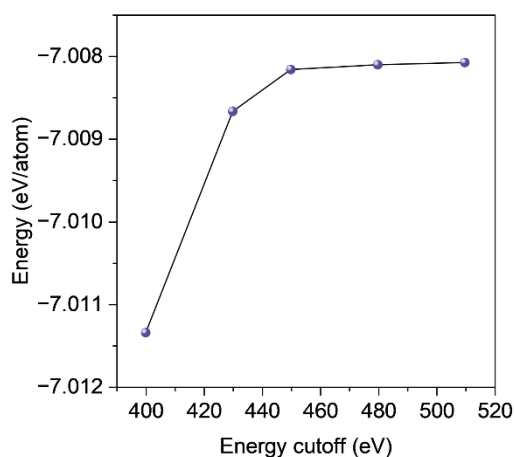


**Fig. R15** Convergence tests: plane-wave energy cutoff

4. K-Point mesh of  $2 \times 2 \times 1$  k-mesh may not be sufficient. author should do a convergence test for the K-Point mesh.

**Response:**

Thanks to your comments, we have added the convergence test data for k-mesh (Fig. R16). The relevant data have been added to **Supporting Information** (Fig. S26 shown as Fig. R15), and an additional citation is given in **line 637-638 of the revised manuscript**: "...Convergence test data are shown in Fig. S26."

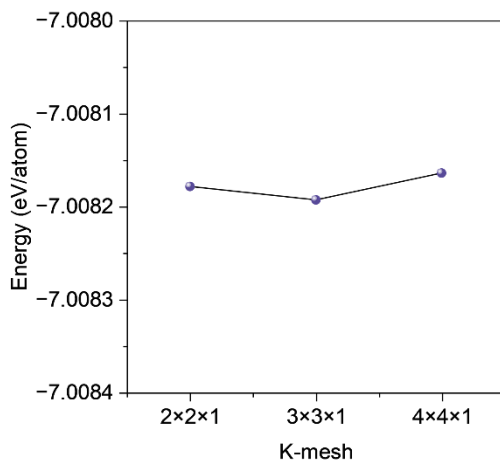


**Fig. R16** Convergence tests: k-point mesh.

5. Author should mention the value of zero point energy and entropy correction in Equ\_10.

**Response:**

Thank you for the suggestion. We have updated Eq. 10 to explicitly include the zero-point energy (ZPE) and finite-temperature corrections (Table. R1), and add a description **in line 658-659 of the revised manuscript**:

$$\Delta G_{H^*} = E_{H^*} - E_{surface} - \frac{1}{2}E_{H_2} + \Delta E_{ZPE} + \Delta U(0 \rightarrow T) - T\Delta S_H \quad (R6)(10)$$

where ... entropic contributions. **Detailed data are presented in Table. S4 (shown as Table. R1).**

**Table. R1** Gibbs free energy calibration data

Lattice strain	0% (eV)	3% (eV)	5% (eV)	7% (eV)	9% (eV)
$E_{H^*}$	-488.00	-485.92	-485.34	-486.59	-483.75
$E_{surface}$	-483.78	-481.977	-481.41	-482.67	-479.75
$\Delta E_{ZPE} +$ $\Delta U(0 \rightarrow T)$	0.21	0.21	0.20	0.20	0.21

$T\Delta S_H$	0.02	0.02	0.01	0.01	0.02
$\Delta G_{H^*}$	-0.61	-0.35	-0.33	-0.32	-0.40

6. Surprisingly, reference for the VASP code as well as exchange correlation functionals are missing.

**Response:**

Thank you for pointing out the shortcomings for us, and we have added relevant literature citations in the **revised manuscript (line 631-636)**:

Additional standard calculations were conducted with the Vienna Ab initio Simulation Package (VASP)[57]. A plane-wave cutoff energy of 450 eV was used, with a convergence criterion of 0.01 eV/Å. The Perdew-Burke-Ernzerhof (PBE) functional within the Generalized Gradient Approximation (GGA) framework handled exchange-correlation interactions[58].

[57]Kresse G, Furthmüller J. Efficiency of ab-initio total energy calculations for metals and semiconductors using a plane-wave basis set. Computational materials science, 1996, 6(1): 15-50.

[58]Perdew J P, Burke K, Ernzerhof M. Generalized gradient approximation made simple. Physical review letters, 1996, 77(18): 3865.

7. Force convergence criteria of 0.02 eV/Å may not be very accurate-author should at least take 0.01 eV/Å.

**Response:**

We have re-structured relaxation and free energy calculations at 0.01 eV/Å for the structure of H\* adsorbed at different strains and have updated the free energy calculation data in the **revised manuscript** (Fig. 4g shown as Fig. R17).

We have updated the description in the **revised manuscript (line 632-633)**: “A plane-wave cutoff energy of 450 eV was used, with a convergence criterion of 0.01 eV/Å.”

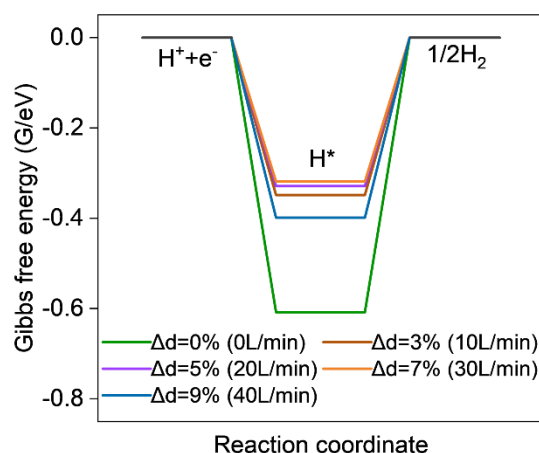


**Fig. R17** Reaction free energies for H adsorption at the top site of the Pt NPs under different lattice strains.

8. Authors mentioned that, “each configuration running for 1,000 steps before incrementally expanding the lattice by 2% biaxially”- Is 1 ps (1000 fs) is enough to reach equilibrium before increasing the strain.

**Response:**

Thank you for the comments. We assessed equilibration by monitoring the AIMD potential-energy trace at each strain and required a stationary fluctuation window before applying the next +2% biaxial increment. The simulation process is divided into 4 phases (Fig. S16 shown as Fig. R18):

1. 5% strain (Fig. R18a): After an initial pre-equilibration, the potential energy fluctuates within  $\pm 0.1$  Hartree over the final 1 ps (1000 steps at 1 fs), indicating a steady state.
2. Transition at 7% (Fig. R18b): An energetic step is observed between 1450–1650 fs, corresponding to a Pt–ligand (Pt–N  $\rightarrow$  Pt–C) coordination change. The event completes within  $\sim 200$  fs, after which the energy returns to stationary fluctuations within the subsequent 300 fs window.
3. 7–9% strain (Fig. R18c): No further structural transitions are detected; the energy remains within  $\pm 0.1$  Hartree, satisfying our stability criterion.
4. 11% strain (Fig. R18d): A sharp energy drop at  $\sim 3500$  fs marks fracture of the COF ring network, as discussed in the manuscript.

Together, these traces show that 1 ps of pre-equilibration at each strain increment

is sufficient to reach a stationary regime, and that any strain-induced rearrangements occur on sub-picosecond timescales and are captured before the next increment.

The above description has been added to the **Theory and Formula of the Supporting Information (page 4)**.

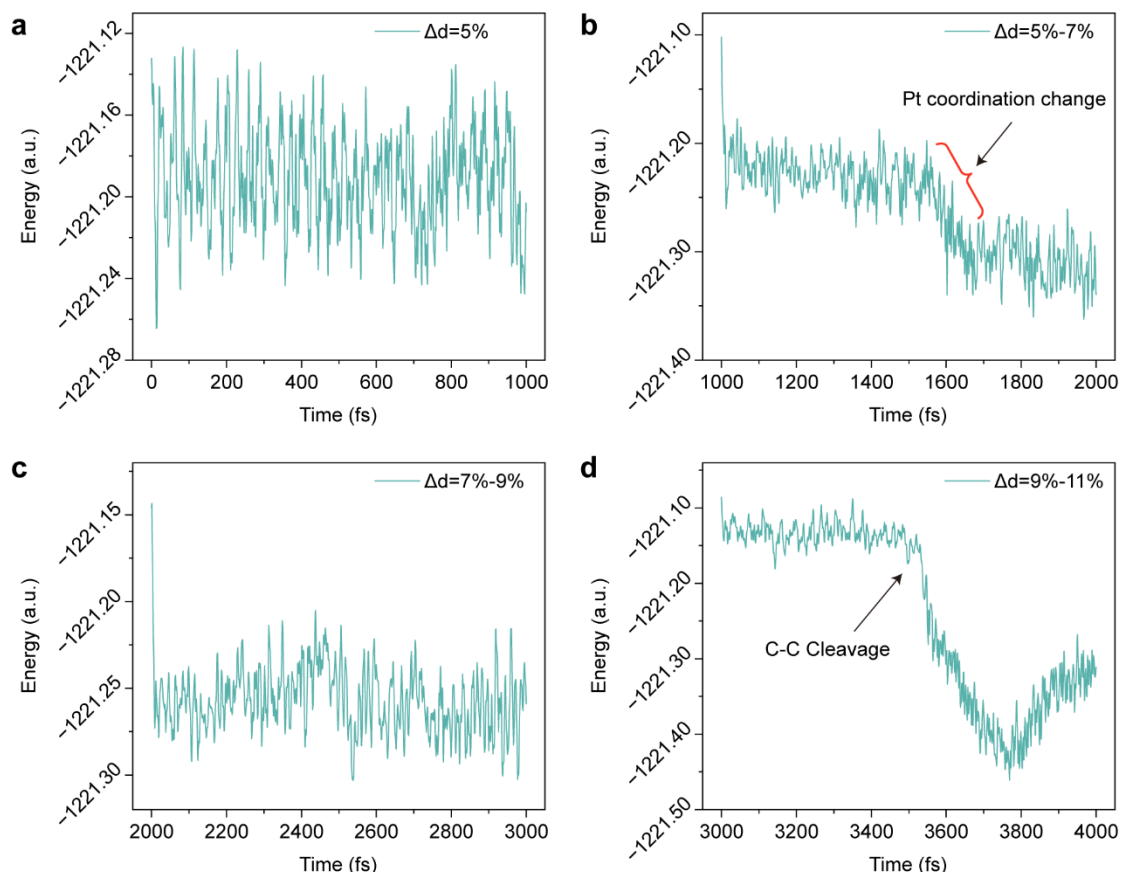


**Fig. R18** Potential-energy fluctuations during AIMD under tensile strain: (a) 5%, (b) 7%, (c) 9%, (d) 11%.

9. Is 11% strain is within the elastic limit? Is it possible to check dynamic stability at 7% strain through phonon calculations.

**Response:**

We appreciate your suggestion to assess dynamical stability via phonon dispersions. The phonon dispersion at 7% pre-strain exhibits real optical and in-plane acoustic branches, while the flexural ZA-like branch lies marginally below zero across the Brillouin zone, reaching  $-0.22$  THz ( $\sim -7.3$   $\text{cm}^{-1}$ ) at K (Fig. S27 shown as Fig. R19). We attribute this shallow imaginary offset to harmonic/IFC convergence limits under pre-stress in 2D frameworks, rather than a robust soft mode.

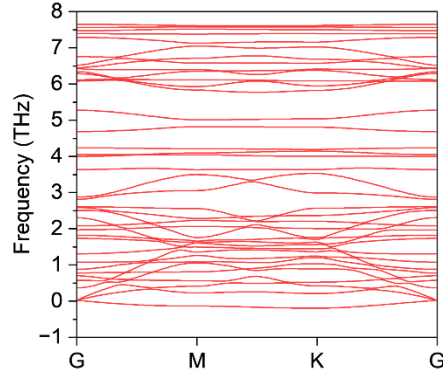


**Fig. R19** Harmonic phonon dispersion of TpPa-COF at 7% strain.

To provide a mechanics-consistent validation beyond the 0 K harmonic limit, we further establish incremental (tangent) stability under the actual pre-stress and confirm finite-temperature dynamical stability via AIMD. Accordingly, we establish incremental dynamical stability at 7% strain by two standard criteria, accompanied by detailed computational procedures:

(1) Positive-definite tangent 2D stiffness (Born criteria)

Statement of the criterion: At a prescribed pre-strain  $\varepsilon_0$  (cell fixed in-plane; internal coordinates relaxed), the incremental/tangent 2D stiffness  $C^{2D}$  (plane stress) must be positive definite. For an orthotropic 2D membrane in Cartesian axes  $(x, y)$ ,

$$C^{2D} = \begin{pmatrix} C_{11} & C_{12} \\ C_{12} & C_{22} \end{pmatrix}, \quad C_{66} > 0 \quad (\text{R7})$$

and the Born stability conditions are:

$$C_{11} > 0, \quad C_{22} > 0, \quad C_{66} > 0, \quad C_{11}C_{22} - C_{12}^2 > 0 \quad (\text{R8})$$

We compute  $C_{ij}^{2D}$  from VASP stresses:

Using central finite differences about  $\varepsilon_0$  with small Cartesian perturbations (uniaxial  $\pm\Delta$  in  $x$  or  $y$ ; and engineering shear  $\gamma = \pm\Delta_\gamma$ , we obtain:

$$\begin{aligned}
C_{11}^{2D} &\approx -\frac{\sigma_{xx}^{3D}(+\Delta\varepsilon_{xx}) - \sigma_{xx}^{3D}(-\Delta\varepsilon_{xx})}{2\Delta} L_z 10^{-2}, \\
C_{22}^{2D} &\approx -\frac{\sigma_{yy}^{3D}(+\Delta\varepsilon_{yy}) - \sigma_{yy}^{3D}(-\Delta\varepsilon_{yy})}{2\Delta} L_z 10^{-2}, \\
C_{12}^{2D} &\approx -\frac{\sigma_{yy}^{3D}(+\Delta\varepsilon_{xx}) - \sigma_{yy}^{3D}(-\Delta\varepsilon_{xx})}{2\Delta} L_z 10^{-2}, \\
C_{66}^{2D} &\approx -\frac{\sigma_{xy}^{3D}(+\gamma) - \sigma_{xy}^{3D}(-\gamma)}{2\gamma} L_z 10^{-2}.
\end{aligned} \tag{R9}$$

Here  $\sigma_{ij}^{3D}$  are the VASP stresses from the `in kB` block (Table. S1 shown as Table. R2),  $L_z$  is the vacuum-included cell height in Å (here  $L_z = 25$  Å),  $\Delta = 0.002$  ( $\pm 0.2\%$  uniaxial),  $\Delta_\gamma = 0.002$  ( $\pm 0.2\%$  engineering shear) and the factor  $10^{-2}$  converts  $\text{kB} \times \text{\AA}$  to N/m since  $1 \text{ kB} = 108 \text{ Pa}$ .

**Table. R2** Raw stresses from OUTCAR (kB)

Case	$\sigma_{xx}$	$\sigma_{yy}$	$\sigma_{xy}$
Baseline	-8.55903	-8.57052	-1.79438
x + 0.2%	-8.70080	-8.55234	-1.79010
x - 0.2%	-8.38975	-8.54638	-1.79966
y + 0.2%	-8.54441	-8.70824	-1.79026
y - 0.2%	-8.53642	-8.39349	-1.79968
shear + 0.2% $\gamma$	-8.53774	-8.54705	-1.79601
shear - 0.2% $\gamma$	-8.53760	-8.54624	-1.79568

Tangent 2D stiffness results (N/m):  $C_{11} = 19.44$ ,  $C_{22} = 19.67$ ,  $C_{12} = 0.44$ ,  $C_{66} = 8.68$ , so  $C_{11} > 0$ ,  $C_{22} > 0$ ,  $C_{66} > 0$  and  $C_{11}C_{22} - C_{12}^2 > 0$ , hence  $C^{2D}$  is positive-definite at 7% pre-strain.

## (2) Positive acoustic tensor under the measured pre-stress

Statement of the criterion: At a prescribed pre-strain  $\varepsilon_0$  with in-plane pre-stress  $\tau^{2D}$ , incremental dynamical stability requires the acoustic tensor

$$\Gamma_{ik}(\mathbf{n}) = \frac{1}{\rho_{2D}} (C_{ijkl}^{2D} n_j n_l + \tau_{jl}^{2D} \delta_{ik} n_j n_l) \tag{R10}$$

to be positive definite for every in-plane direction  $\mathbf{n} = (\cos\theta, \sin\theta)$ ; equivalently,



both eigenvalues  $v_m^2(\theta)$  are positive (real wave speeds) for all  $\theta \in [0, 2\pi)$ .

Directional form for an orthotropic 2D membrane. (With Voigt notation)

$$\mathbf{C}^{2D} = \begin{pmatrix} C_{11} & C_{12} & 0 \\ C_{12} & C_{22} & 0 \\ 0 & 0 & C_{66} \end{pmatrix}, \quad \boldsymbol{\tau}^{2D} = \begin{pmatrix} \tau_{xx} & \tau_{xy} \\ \tau_{xy} & \tau_{yy} \end{pmatrix} \quad (\text{R11})$$

define  $s(\theta) = \mathbf{n}^T \boldsymbol{\tau}^{2D} \mathbf{n}$ . The projected stiffness entering  $\Gamma$  is

$$\mathbf{n} : \mathbf{C}^{2D} : \mathbf{n} = \begin{pmatrix} C_{11} \cos^2 \theta + C_{66} \sin^2 \theta & (C_{12} + C_{66}) \sin \theta \cos \theta \\ (C_{12} + C_{66}) \sin \theta \cos \theta & C_{22} \sin^2 \theta + C_{66} \cos^2 \theta \end{pmatrix} \quad (\text{R12})$$

so that  $\rho_{2D} \Gamma(\mathbf{n}) = (\mathbf{n} : \mathbf{C}^{2D} : \mathbf{n}) + s(\theta) \mathbf{I}_2$ . The requirement “ $\Gamma(\mathbf{n}) > 0$  for all  $\theta$ ” is exactly the wave-propagation (WP) / strong-ellipticity condition used today to certify incremental stability under finite pre-stress.

Verification (direction-independent lower bound)

The smallest eigenvalue of the in-plane block is

$$\lambda_{\min}(\mathbf{C}^{2D}) = \frac{C_{11} + C_{22} - \sqrt{(C_{11} - C_{22})^2 + 4C_{12}^2}}{2} \approx 19.1 \text{ N/m} > 0.$$

For any  $\theta$ , with  $s(\theta) \in [-2.15, -2.13] \text{ N/m}$ ,

$$\lambda_{\min}(\rho_{2D} \Gamma(\mathbf{n})) \geq \lambda_{\min}(\mathbf{C}^{2D}) + s(\theta) \gtrsim 19.1 - 2.15 = 16.9 \text{ N/m} > 0.$$

Therefore,  $\Gamma(\mathbf{n})$  is positive for all directions, implying real incremental wave speeds and establishing incremental dynamical stability at 7% pre-strain.

These mechanics-based results are consistent with our finite-temperature AIMD at strains  $\leq 7\%$ , which show no spontaneous reconstruction or bond scission over the simulation windows, while fracture occurs only near  $\sim 11\%$ . Together, they define a physically meaningful stability window of 0–7% strain for the COF considered here.

We will clarify this rationale and add a concise description of the incremental-stability procedure (with equations and the numerical values above) in the **Theory and Formula of the Supporting Information (page 4)**.

10. For the AIMD structures, author need to show energy fluctuation and bond length fluctuations with different strain.

**Response:**

Thank you for the suggestion. We have added time-resolved AIMD energy fluctuations and bond-length trajectories under different in-plane strains. Specifically, Fig. S16 (shown as Fig. R18) shows the total potential-energy traces for each strain window, and Fig. S18 (shown as Fig. R20) presents the instantaneous Pt–N and Pt–C bond lengths between the Pt cluster and the COF ligands during the simulations.

**In the revised manuscript (line 419-429),** we now state: “It has been demonstrated that by tracking the evolution of Pt's positional coordination, it is possible to ascertain that initially, Pt atoms predominantly adopt a Pt–N coordination configuration (with an average Pt–N bond length of approximately 2.1 Å), consistent with  $\kappa^2$ - (N, O) binding of the COF linker. Under 5% in-plane strain, the Pt<sub>4</sub> NPs undergoes a gradual ligand rearrangement toward Pt–C coordination (average Pt–C bond length  $\approx$  2.0 Å), consistent with the evolving interfacial environment (Fig. S14). When  $\Delta d = 11\%$ , the COF aromatic ring network fractures (Fig. S15). The potential energy (Fig. S16) and conserved quantity traces (Fig. S17), together with the time-resolved Pt–N/Pt–C bond-length fluctuations (Fig. S18), quantify these strain-dependent transitions.”

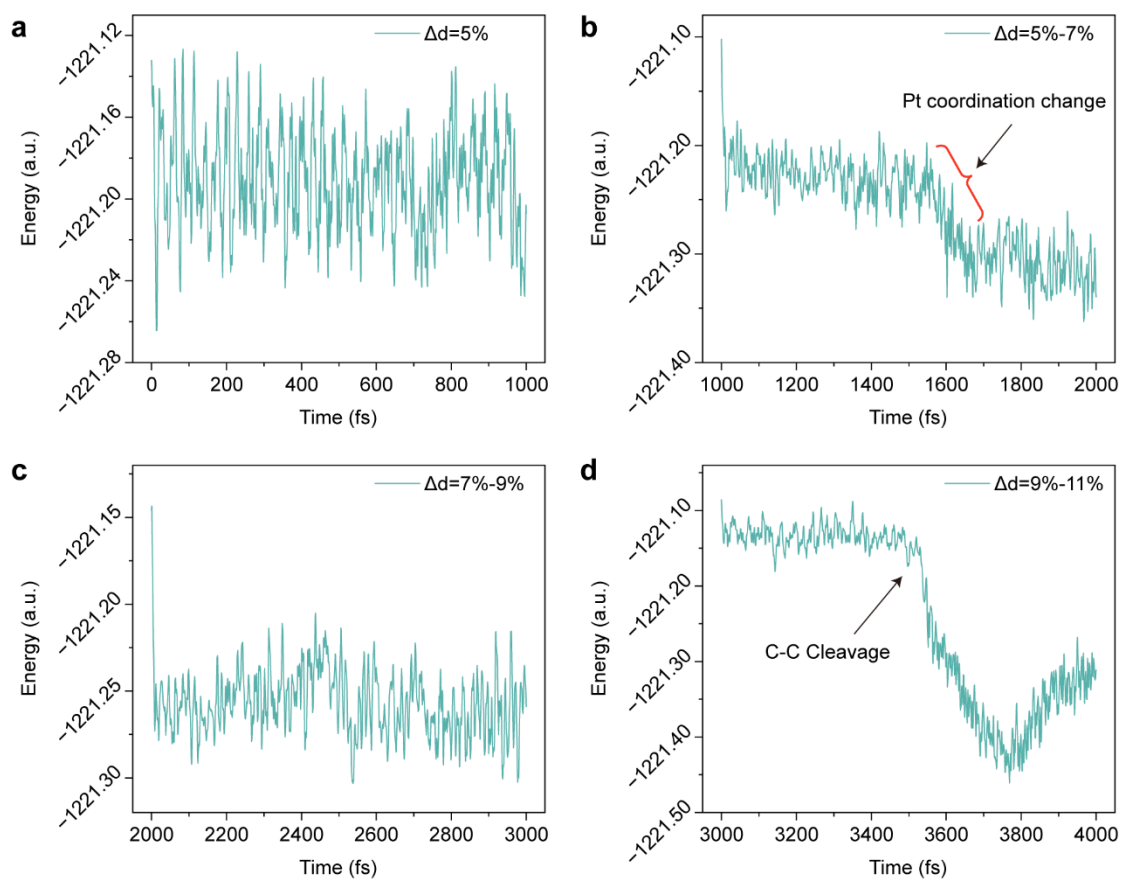


**Fig. R18** Potential-energy fluctuations during AIMD under tensile strain: (a) 5%, (b) 7%, (c) 9%, (d) 11%.

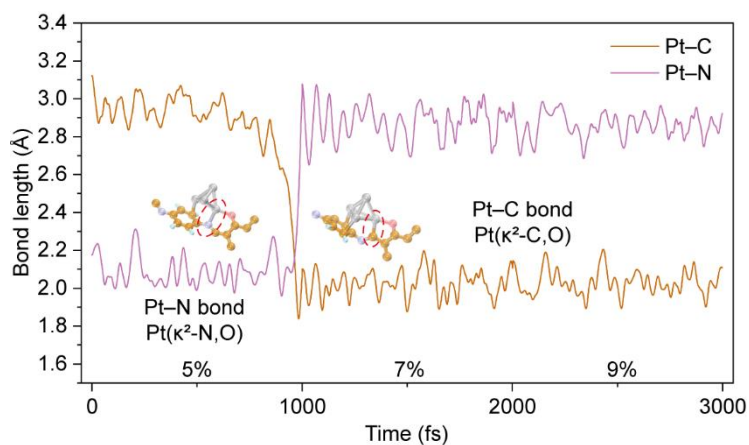


**Fig. R20** Time-resolved Pt-C and Pt-N bond-length variations during AIMD.